The Comoros archipelago: a right-lateral transform boundary between the Somalia and Lwandle plates

Vincent Famin, Laurent Michon, Anli Bourhane

The Comoros archipelago: a right-lateral transform boundary between the Somalia and Lwandle plates

Vincent Famin[a,b,*], Laurent Michon[a,b], Anli Bourhane[c]

[a] Université de Paris, Institut de physique du globe de Paris, CNRS, UMR 7154, F-75005 Paris, France
[b] Université de La Réunion, Laboratoire GéoSciences Réunion, F-97744 Saint-Denis, France
[c] Office de l'eau de La Réunion, F-97400 Saint-Denis, France

A B S T R A C T

The origin of the Comoros archipelago in the Mozambique channel is the subject of a longstanding controversy. This volcanic chain has been successively interpreted as a hotspot track, as built on an intraplate fracture zone or a passive margin, or as the northern limit of a diffuse deformation zone in the Nubia-Somalia plate system, none of these interpretations being entirely satisfactory. It is also possible that the volcanism of the Comoros is a branch of the East African Rift System, and delineates the still poorly constrained northern boundary between the Lwandle and Somalia plates. To better understand the origin of the Comoros archipelago, we combined a formal stress inversion of earthquake focal mechanisms and deformation structures (faults and dykes) observed on three islands (Mayotte, Anjouan, and Mohéli) with a morphologic study of the repartition of onshore and offshore volcanic vents in the area.

Earthquake focal mechanisms and field-observed deformation structures both yield a generalized strike-slip regime with a maximum horizontal stress oriented NW-SE. In tandem, the study of topographic and bathymetric features shows that volcanic vents follow a preferential repartition along two trends: N105 ± 10° lineaments up to 100 km-long, and N145 ± 10°, less than 60 km-long lineaments organized in an *en échelon* fashion. Earthquakes, deformation structures, and volcanic vents all consistently designate the Comoros archipelago as an *E*-W elongated, 150 km-wide zone of right-lateral tear in the lithosphere. Because the clockwise rotation of Somalia relative to Lwandle requires the existence of such a right-lateral shear zone, we interpret the Comoros archipelago as the northern boundary between the two plates. This plate boundary is still in an immature state, which is why it remained undetected until now.

Keywords:
Comoros archipelago ; Mozambique channel ; East African Rift System ; Earthquake focal mechanisms ; Stress inversion ; Paleostress ; Volcanism ; Plate boundary ; Lwandle microplate Somalian plate

1. Introduction

The geodynamics of the Mozambique channel, between East Africa and Madagascar, remains enigmatic in many aspects. One of these aspects is the decomposition of the region into tectonic plates. Plate motion data impose the existence of at least three lithospheric blocks between Nubia and Somalia, Victoria, Rovuma and Lwandle (Horner-Johnson et al., 2007; Stamps et al., 2008), but some of their boundaries are not well constrained (Fig. 1a). For instance, the limit between Lwandle and Somalia has been alternatively drawn along the Davie ridge and central Madagascar (Hartnady, 2002; Saria et al., 2014), along the Comoros and the east passive margin of Madagascar (Stamps et al., 2018), or even as a diffuse deformation zone encompassing most of Madagascar or even the whole Mozambique channel (Horner-Johnson et al., 2007; Stamps et al., 2008; Kusky et al., 2010). The connection of this boundary with the East African Rift System (EARS) that delimits the separation of the Lwandle and Rovuma blocks is also unclear (Fig. 1a).

Related to the difficulty of defining plate boundaries in East Africa, the nature of volcanism in the Mozambique channel is another enigmatic aspect of the regional geodynamics. If the northern boundary of the Lwandle plate runs through the Davie ridge and central Madagascar, then the Geyser and Zélée banks, the Jumelles seamounts, and the Comoros archipelago (including Mayotte, Anjouan, Mohéli and Grande Comore) must be considered as intraplate volcanism affecting Somalia (Fig. 1b). In this category of interpretations, hotspot volcanism is supported by the enriched mantle (EM) signature of the volcanism in Grande Comore (Class et al., 2009 and references therein), and by the apparent younging of islands from Mayotte to Grande Comore that suggests a westward progression of a plume-related volcanism (Hajash

* Corresponding author at: Université de Paris, Institut de physique du globe de Paris, CNRS, UMR 7154, F-75005 Paris, France.
E-mail address: vfamin@univ-reunion.fr (V. Famin).

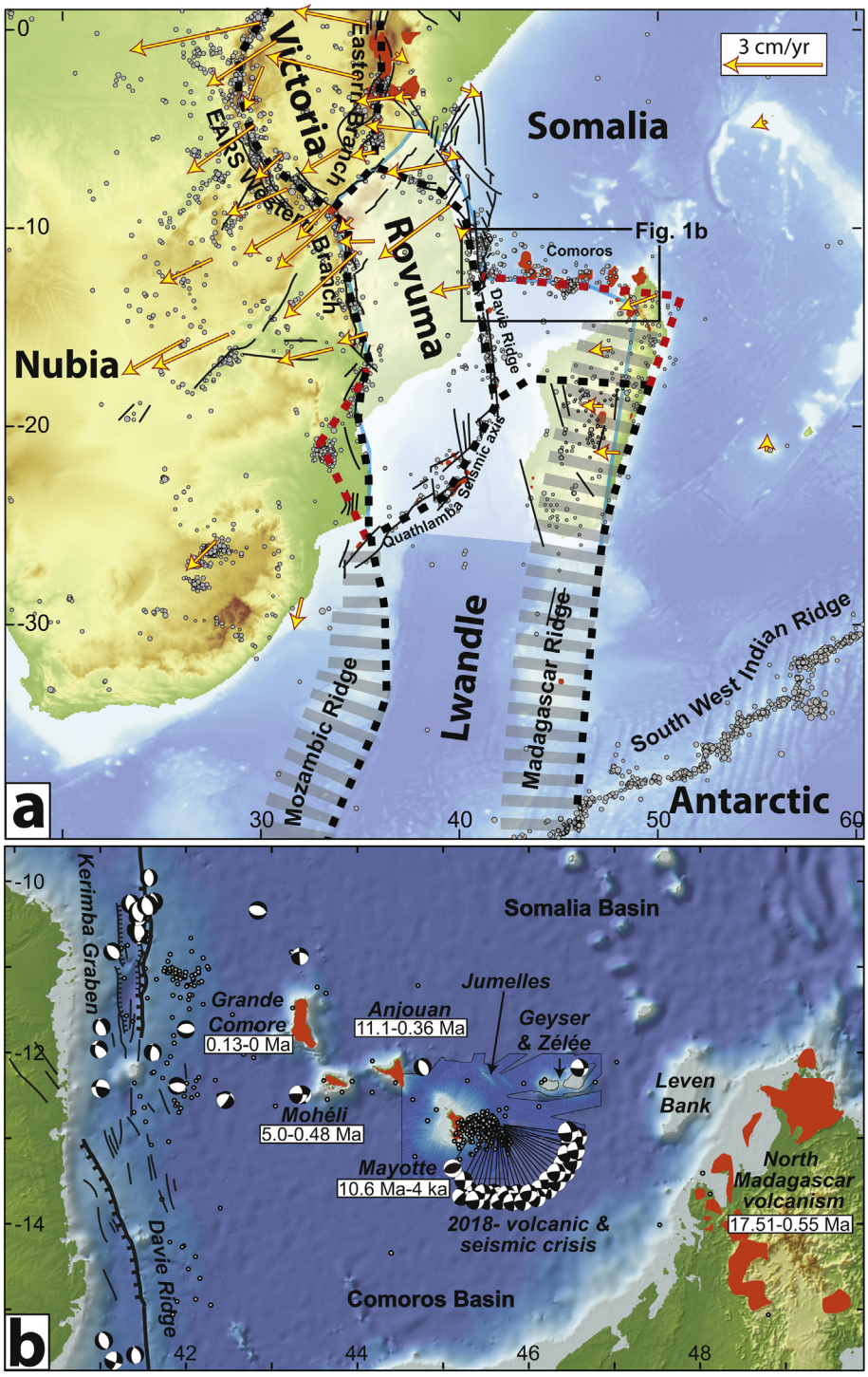

Fig. 1. a) Tectonic map of the western Indian Ocean and the East African Rift System (EARS), showing regional seismicity (NEIC catalogue, USGS), GNSS plate motions in a Somalia-fixed framework (King et al., 2015), Neogene-to-present volcanism (red areas) and major faults (compilations from Michon, 2016; Deville et al., 2018), and proposed plate boundaries (black hatched lines: Saria et al., 2014; red hatched lines: Stamps et al., 2018) or zones of diffuse deformation (grey hatched areas: Stamps et al., 2008; clear blue-framed area: Kusky et al., 2010). b) Volcanic seamounts and islands of the Comoros archipelago. Active faults from Franke et al., (2015); Deville et al., (2018) and earthquake focal mechanisms from the Global CMT Catalogue (Dziewonski et al., 1981; Ekström et al., 2012) and from Barth et al. (2007). Compilations of Neogene-to-present volcanic ages from Pelleter et al., (2014); Cucciniello et al., (2016). Elevation/bathymetry grids are from SHOM, 2016) in the Mayotte area and from GEBCO elsewhere. (For interpretation of the references to colour in this figure legend, the reader is referred to the web version of this article.)

and Armstrong, 1972; Emerick and Duncan, 1982). However, this *E*-W volcano trail does not match the northward or NNW-directed absolute motions of the Somalia and Lwandle plates (Morgan and Phipps Morgan, 2007; Wang et al., 2018). Continental xenoliths found in volcanic rocks from the four islands support the idea that the Comoros archipelago may be built on a stretched passive margin (Montaggioni and Nougier, 1981). For this reason, and because more recent geochronological works dispute the proposed age progression of volcanism (Nougier et al., 1986; Pelleter et al., 2014), it has been proposed that the Comoros volcanism might be controlled by reactivation of crustal structures linked to the continent-ocean transition (Nougier et al., 1986), possibly in relation with the EARS (Michon, 2016). A third, more recent hypothesis is to consider the Geyser-to-Grande Comore volcanic alignment (hereafter called GCVA) as the northern limit of the Lwandle plate connecting the EARS to the Tertiary-to-Quaternary volcanism and rifting of Madagascar (Stamps et al., 2018). Growing earthquake catalogues show that the GCVA is indeed a zone of focused seismicity (Bertil and Regnoult, 1998; Rindraharisaona et al., 2013), and thus a potential plate boundary (Fig. 1a). The nature of this hypothetic boundary, its kinematics, and the reason why it concentrates volcanism, remain to be elucidated.

The seismic crisis initiated 20 to 50 km east of Mayotte in May 2018 (Fig. 1b), still ongoing at the time of writing (REVOSIMA, 2020), associated with magmatic activity and the birth of a new submarine

volcano (Feuillet et al., 2019; Cesca et al., 2020), reactivates the controversy about the nature of the Comoros volcanism. Is the GCVA a plume-related intraplate hotspot trail, a zone of volcanic rifting, and/or a plate boundary? Answering this question is critical, not only for a fundamental understanding of the regional kinematics, but also for a practical assessment of the hazards represented by the ongoing volcanic and seismic crisis. Hence, we combine a formal stress inversion of earthquake focal mechanisms in the area, a field survey of deformation meso-structures and intrusions in Mayotte, Anjouan and Mohéli, and a mapping of onshore and offshore volcanic cones along the GCVA based on digital surface models. Added to the existing knowledge, the observation facts described in this paper allow us to propose a new tectonic interpretation of the GCVA, and an answer to the above questions.

2. Regional geology

A large part of the controversy about the nature of the GCVA revolves around the existence, or absence, of a progression of volcanism along the chain. The Leven and Geyser & Zelée banks are volcanic seamounts very likely related to Neogene-to-present volcanism (Fig. 1b), but the age of these structures is unknown (Daniel et al., 1972; Maugé et al., 1982). Radiometric ages of 10.6 Ma to 4 ka on Mayotte, 11.1 Ma to 360 ka on Anjouan, 5 Ma to 480 ka on Mohéli, and 130 to 0 ka on Grande Comore (Pelleter et al., 2014 and references therein), neither support nor refute such a progression, unless the Neogene-to-Quaternary volcanism of northern Madagascar (17.5 to 0.55 Ma) is included in the chain (Fig. 1b). Nevertheless, the eroded shape and well-developed fringing reef of Mayotte and the active Karthala volcano in Grande Comore suggest a westward younging of volcanism. The formation of a new volcano in 2018, 50 km east of Mayotte on the ocean floor, contradicts this apparent volcanic age progression. Despite this lack of hotspot trail chronology, a true mantle plume Sr-Nd-Pb-Os-He isotopic signature is evidenced in the volcanism of the Grande Comore showing EM and depleted MORB mantle (DMM) contributions (see reviews by Class et al., 2009 and Pelleter et al., 2014). This mantle source is not obvious on the other islands of the GCVA dominated by DMM and HIMU signatures, which suggests more lithospheric (either oceanic or continental) magma sources. North of the GCVA, the seafloor shows a typical oceanic fabric with magnetic anomalies starting at M24Bn (152.43 Ma) and becoming symmetric around a paleo-ridge axis from M18r (141.22 Ma) to M0r (120.8 Ma) (Davis et al., 2016). South of the GCVA, in the Comoros basin, the nature of the crust is unclear, with neither well-defined magnetic anomalies nor obvious free air gravity structures (Phethean, 2016). With such uncertainties, it is possible that the continental passive margin of northern Madagascar may extend northward up to the GCVA, as suggested by the detrital xenoliths found on all the Comoros islands (Esson et al., 1970; Flower, 1972; Montaggioni and Nougier, 1981).

The subaerial volcanism of Mayotte may be subdivided into five main stages (Nehlig et al., 2013): (1), A substratum basanitic volcanism from the middle Miocene to 5 Ma present on the south of the island; (2) two primitive shields from 5 to 3.2 Ma on the north-eastern and southern parts of the island, respectively (Phases I and II); (3) more differentiated lavas from 2.9 to 1.2 Ma in the centre and south (Phases III and IV); (4) Strombolian basaltic and basanitic volcanism in the north from 0.8 to 0.2 Ma (Phase V); (5) very recent (200 to 4 ka) phonolitic phreatomagmatism with well-preserved maar structures on Petite Terre and in the northeast (Phase VI). The subaerial construction of Anjouan and Mohéli may described by a roughly similar chronology (Nougier et al., 1986): older series of basanites and nephelinites prior to 5 Ma, middle series of ankaramites, basanite and hawaiites from 4 to 2.5 Ma; younger series of basanites to nephelinites from 2.5 to 1.5 Ma, and recent Strombolian volcanism since 0.8 Ma.

Based on earthquake focal mechanisms, fault-slip data, and borehole breakouts from the World Stress Map in the East Africa and Mozambique channel area (Heidbach et al., 2010), the GCVA is interpreted as the limit between two stress regimes with a NW-SE maximum horizontal stress (S_{Hmax}), dominantly strike-slip to the north and extensional to the south (Bird et al., 2008; Ghosh and Holt, 2012). Even before the 2018 volcanic and seismic crisis, seismicity was already occurring in the vicinity of Mayotte along the GCVA. The ongoing crisis associated with the new submarine volcano has strongly increased the level of seismicity, with earthquakes of magnitude up to 5.9 (Lemoine et al., 2020).

3. Methods

The first approach used in this study is a formal stress inversion of earthquake focal mechanisms, and of markers of rock deformation (mostly fault-slip data) and planar intrusions measured in the field. Earthquake focal mechanisms come from the Global Centroid-Moment-Tensor (GCMT), which routinely determines focal mechanisms by moment tensor inversion of both long period body- and surface-waves for $M_w \geq 4.7$ earthquakes (Dziewonski et al., 1981; Ekström et al., 2012). Deformation meso-structures are observed at the outcrop scale and include faults with striated surfaces and/or observed slip sense (normal, inverse, dextral or sinistral), and extension fractures. Intrusions measured in the field are planar dykes or sills considered to have formed as extension fractures filled with magma, even though a shear component may occur in some intrusions. Deformation and intrusion data were manually sorted into subsets, based firstly on field-observed chronological criteria such as crosscutting relationships, and based secondly on their orientation. A confidence level was attributed to each deformation marker (certain, probable, supposed, unknown) using the conventions of fault-slip analysis (Angelier, 1984; Delvaux and Sperner, 2003; Sperner et al., 2003; Sperner and Zweigel, 2010).

Stress orientations were obtained by separate and independent inversions of earthquake focal mechanisms, deformation structures, and intrusions, following procedures described in Delvaux and Sperner (2003) and Delvaux and Barth (2010), and briefly recalled here. These stress inversion methods are based on a number of assumptions (stresses coaxial to strains; small displacements on fractures and focal planes compared to the volume of the rock mass; no interaction between fractures; intrusions opened as extension fractures without slip; slip vector colinear to maximum shear stress on fault and focal planes), which have proven to be reasonable in practice (Lacombe, 2012). Earthquake focal mechanisms and deformation structures allow reconstructing a reduced stress tensor composed of four parameters, the three orthogonal directions of principal stresses ($\sigma_1 \geq \sigma_2 \geq \sigma_3$) and the ratio $R = (\sigma_2 - \sigma_3)/(\sigma_1 - \sigma_3)$. Intrusions only provide the direction of the least principal stress (σ_3). While earthquake inversion yields an estimate of the present-day stress field over a given region, deformation markers and intrusions provide “paleostresses”, i.e. stresses that occurred in the past after the emplacement of rocks.

For the inversion, we used the Rotational Optimization Method of the Win-Tensor software (Delvaux and Sperner, 2003). This iterative inversion method consists in finding the orientations of principal stresses that satisfy the following conditions: (1) for focal planes and faults, maximizing the resolved shear stress magnitude and minimizing the resolved normal stress magnitude to favor slip, while minimizing the averaged deviation between observed and computed slip vectors on each nodal/fault plane; (2) for extension fractures, minimizing both the normal stress and the shear stress to favor opening and prevent slip. For stress tensors deduced from focal mechanisms and deformation data, the horizontal maximum and minimum stress orientations (S_{Hmax} and S_{hmin}, respectively) and their 1σ standard deviation were computed from the values and uncertainties of the four parameters of the reduced stress tensor using the method of Lund and Townend (2007). As only the orientation of σ_3 is known from the inversion of intrusions, S_{hmin} and S_{Hmax} deduced from these data were computed as the projection of the σ_3 axis in the horizontal plane and its perpendicular, keeping in mind that such projection may yield erroneous results whenever two

principal stress magnitudes are close to each other.

The procedure used for the inversion of focal mechanisms is the one developed by Delvaux and Barth (2010). Focal mechanisms were sorted into subsets in which the stress field is considered as uniform and invariant in space over the selected area, and in time over the duration of seismicity. Here we considered two subsets, one encompassing focal mechanisms occurring over the GCVA for the period 1976–2017, the other associated with the 2018 seismic crisis east of Mayotte. Within each subset, inversion was made in two steps. In the first step, focal mechanisms were inverted into a preliminary reduced stress tensor using their two nodal planes. The nodal plane of each focal mechanism that is best explained by this preliminary stress tensor was then selected as the true fault plane. In the second step, the final inversion was performed by finding the best reduced stress tensor fitting the subset of selected nodal planes. The quality of the final reduced stress tensor was estimated using the quality index (QR_{fm}) for focal mechanisms of the World Stress Map Project (Heidbach et al., 2010, 2018), ranging from A (best quality) to C (worst) in the case of $M \geq 2.5$ earthquakes:

QR_{fm} = A for S_{Hmax} within ± 15°, number of data $n \geq 15$, and average slip deviation $\alpha_{aver} \leq 12°$;

QR_{fm} = B for S_{Hmax} within ± 15–20°, $8 \leq n < 15$, and $12 < \alpha_{aver} \leq 20°$;

QR_{fm} = C for individual earthquakes, or for subsets with S_{Hmax} within 20–25°, $n < 8$, and $\alpha_{aver} > 20°$.

The procedure for the inversion of deformation and intrusion data was also designed in two steps in order to allow inter-comparison of paleostress tensors with earthquake-derived stress tensors. In the first step, inversion was performed on subsets corresponding to each outcrop, by processing separately deformation and intrusion data. This separated inversion has the advantage of allowing a comparison of magmato-tectonic and purely tectonic strain markers. The quality of these outcrop-scale reduced paleostress tensors was estimated using two indexes ranging from A (best) to E (worst), as defined by Delvaux and Sperner (2003). The first index, QR_w, rates the quality of principal stress orientations, depending on (1) the number of data per tensor n, (2) the proportion of data used in the tensor relative to the total number of data measured at each outcrop n/n_t, (3) the average slip deviation α_{aver}, (4) the average confidence level of the subset of deformation markers CL_w, and (5) the average type of data used for tensor determination DT_w, based on the usefulness of each deformation marker in stress inversion (1 for striated faults; 0.5 for tension fractures or dykes, and 0.25 for faults with slip sense but no striation). The second index, QR_T, rates the quality of R estimates using all the criteria of QR_w, plus two criteria related to the diversity of fault planes (Delvaux and Sperner, 2003). In the second inversion step, outcrop-scale paleostress tensors (from deformation or intrusion data) were considered as "paleo-earthquake focal mechanisms", sorted into three subsets (Mayotte, Anjouan, and Mohéli), and weighted according to their QR_w quality. Final inversions were run on these three subsets following the same procedure as for focal mechanisms, hence using the quality criterion QR_{fm}.

To compare our stress inversion with geomorphic data, we also mapped the onland and offshore repartition of monogenic volcanic cones. This repartition was assessed by manually picking volcanic cones on two types of digital surface models (DSM): the ALOS World 3D – 30 m DSM for Mayotte, Anjouan, Mohéli and Grande Comore onshore (Tadono et al., 2014), and a 100 m-resolution digital bathymetric model from the Service Hydrographique et Océanographique de la Marine for Mayotte offshore (SHOM, 2016). Although used in figures, the GEBCO elevation/bathymetric grid was not used for mapping of individual volcanic cones because of its too low resolution. The identification of volcanic alignments was made with the procedure of Paulsen and Wilson (2010). This procedure starts by constructing best-fit ellipses to match the shape of each vent, in order to take the elongation of monogenic cones into account. Volcanic alignments are then preliminarily defined by drawing a line through the long axes of a series of elongated vents, and/or through circular vents that are in clear visual alignment because of their close spacing distance (≤ 1 km). The final best-fit line is then calculated by minimizing the orthogonal distance between the centres of the ellipses and the line (i.e. Deming regression analysis). The reliability of vent alignments determination was classified in four grades (A > B > C > D) based on (1) the number of vents ($A \geq 25$, $B \geq 15$, $C \geq 10$, $D \geq 8$), (2) the standard deviation of vent centres from the best-fit line using the grades of Suter et al. (1992) (A < 750 m, B < 1500 m, C ≤ 2250 m, D > 2250 m), (3) the average shape ratio of elongated vents ($A \geq 1.4$, $B \geq 1.3$, $C \geq 1.2$, $1.2 > D > 1$), and (4) their average angular deviation from the best-fit line ($A \leq 30°$, $B \leq 35°$, $C \leq 40°$, $D > 40°$).

4. Results

4.1. Earthquake focal mechanisms

The GCMT catalogue contains 33 earthquake focal mechanisms for the GCVA area over the 1976–2019 period, all of them occurring at lithospheric depth ≤ 68 km (Table S1). Of this dataset, 28 focal mechanisms belong to the 2018- crisis whereas only five events occurred earlier in 2000, 2007, 2011, 2012, and 2016. All but one of the 2018-focal mechanisms are in strike-slip stress regime, and are located in the vicinity of the new submarine volcano, ~50 km offshore east of Mayotte. The remaining one, occurring in 2019, is in compression. Four of the five focal mechanisms available for the 1976–2017 period are also of the strike-slip regime, the remaining one being extensional. These five focal mechanisms occur across all the GCVA, near the Geyser bank, northeast of Anjouan, southwest of Mohéli, and north of Grande Comore.

Stress tensors deduced from the inversion of earthquake focal mechanisms are provided in Table 1. Focal mechanisms from the 2018-crisis yields a reduced stress tensor of the best quality (QR_{fm}: A), corresponding to a strike-slip stress regime with an S_{Hmax} oriented

Table 1
Summary of stress and paleostress tensor parameters for the Comoros archipelago.

Subset definition		Reduced stress tensor parameters						Statistics and quality rank			
No	Location	σ_1 dip/dip direction	σ_2 dip/dip direction	σ_3 dip/dip direction	R	S_{Hmax} (°)	Stress regime[a]	α_{aver} (°)	α_{max} (°)	n/n_t	QR_{fm}
Earthquake focal mechanisms											
1	2018- crisis	14/322	59/077	27/224	0.8	135 ± 13.4	SS	6.6 ± 4.8	15.7	28/28	A
2	1976–2017	35/316	51/165	14/057	0.2	139 ± 6.8	SS	5 ± 2.7	8.2	5/5	C
Paleostresses											
3	Mayotte	01/161	81/260	09/071	0.1	160 ± 6.4	SS	11.7 ± 9.6	36.6	22/24	A
4	Mayotte	01/254	63/162	27/345	0.25	074 ± 9.5	SS	6.5 ± 4	13.7	7/9	C
5	Anjouan	72/139	16/351	09/258	0.55	166 ± 9.1	NF	8.5 ± 7.5	24.3	7/9	C
6	Mohéli	48/358	31/128	26/235	0.01	178 ± 4.8	NS	11.4 ± 13.9	34.5	4/5	C

[a] Abbreviations TF, SS, NF, NS refer to thrust, strike-slip, normal, and hybrid normal/strike-slip faulting, respectively.

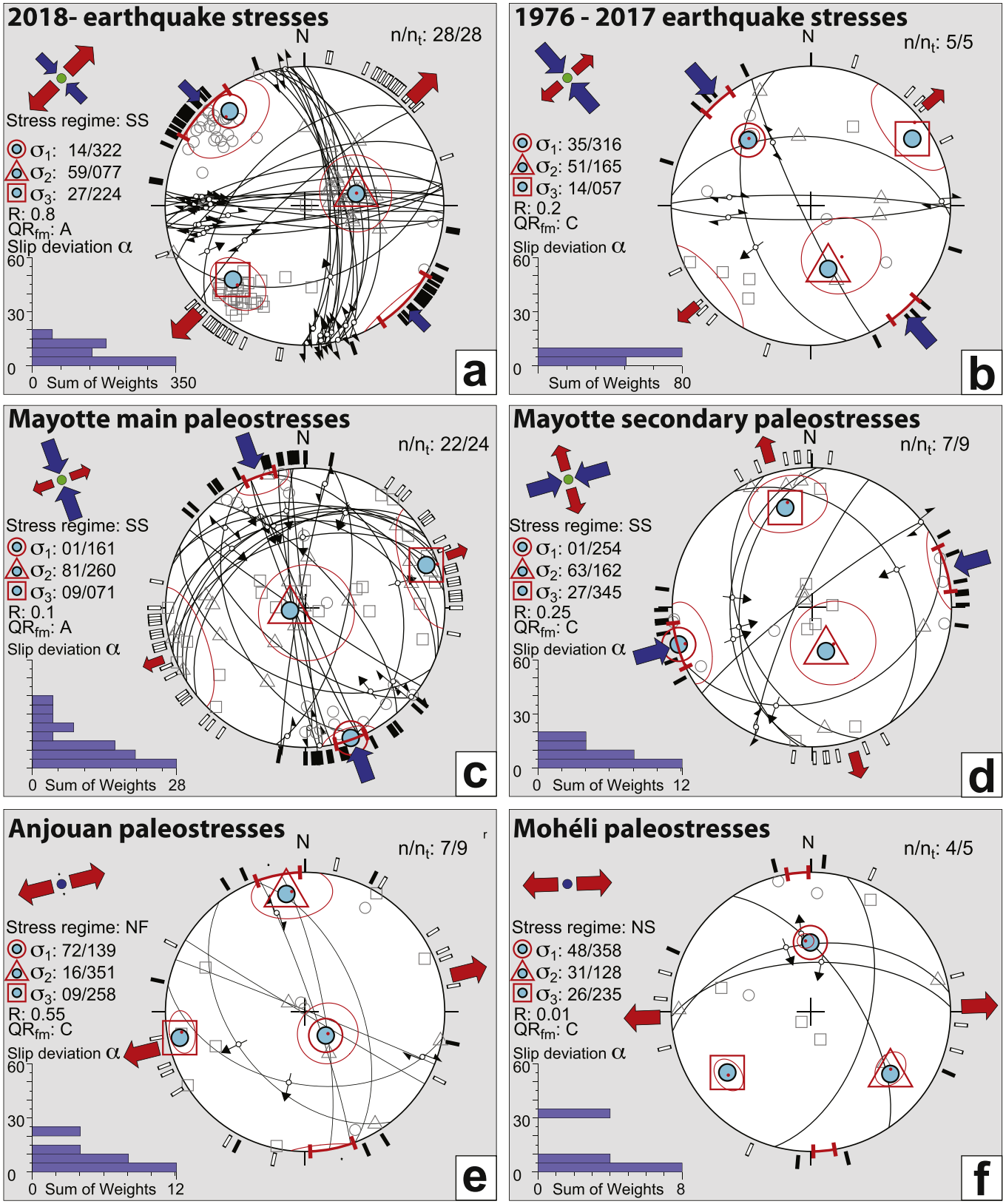

Fig. 2. Average stress and paleostress tensors obtained by inversion of a) earthquake focal mechanisms from the 2018- seismic and volcanic crisis, b) focal mechanisms for the 1976–2017 period, c) quality (QR_w)-weighted paleostress tensors from the dominant population of deformation and intrusion data found all over Mayotte, d) quality-weighted paleostress tensors from the minor population of deformation structures in central Mayotte, e) and f) quality-weighted paleostress tensors for Anjouan and Mohéli, respectively. Abbreviations SS, NF, NS refer to strike-slip, normal and hybrid faulting, respectively. Stereo diagrams are equal area projections, lower hemisphere.

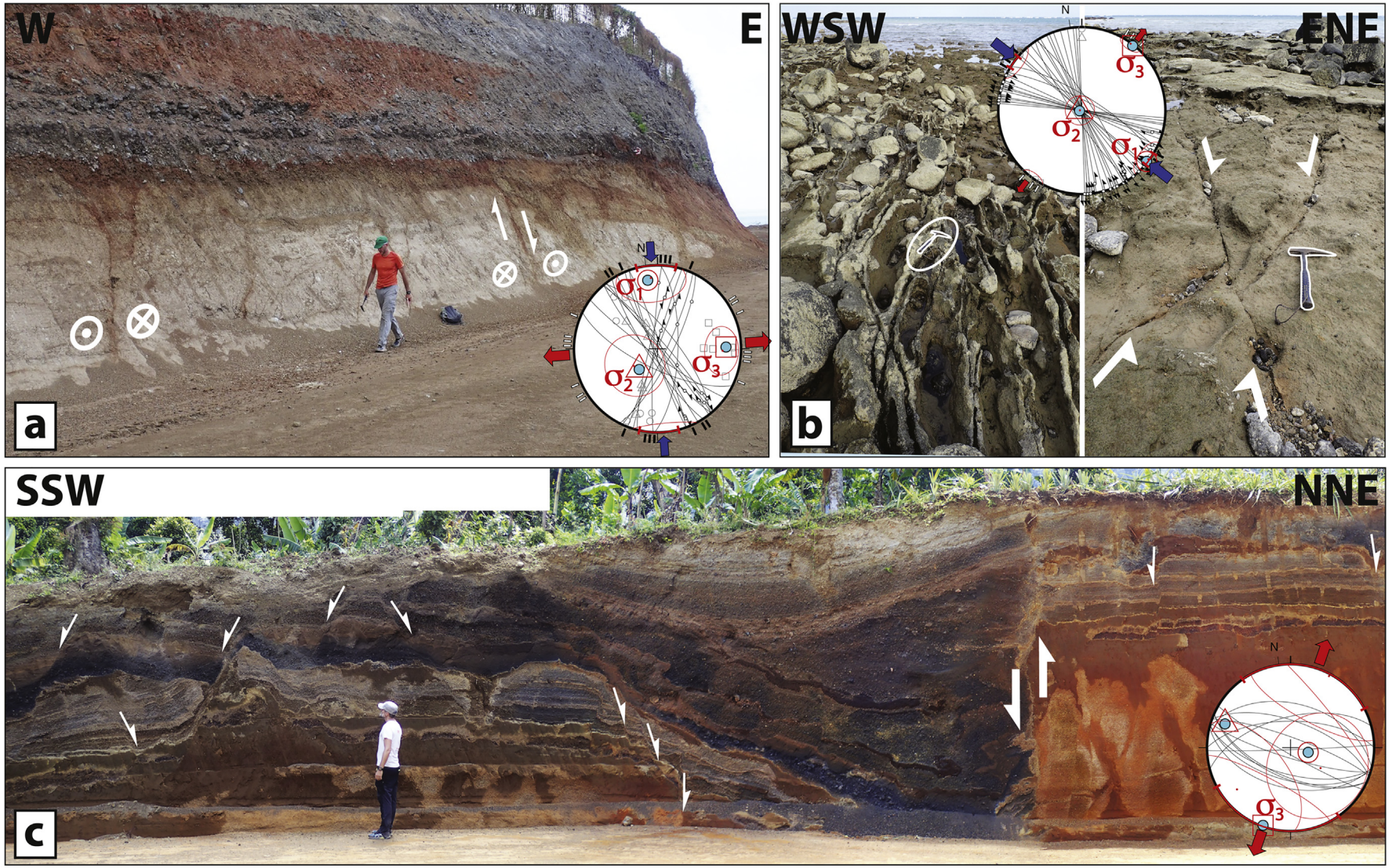

Fig. 3. Examples of deformation structures observed in the field and their paleostress inversions (see Table 2 for tensor parameters and Table 2, Fig. 4 for outcrop locations). a) Dominantly strike-slip faults in intensely deformed altered breccia above a phonolite dome associated with the phase IV of Mayotte. Faults are capped by underformed, phase V Strombolian deposits (site MA16, Kangani quarry). b) Strike-slip faults observed at low tide in phreatomagmatic deposits aged of 200 to 4 ka (site MA50, Pamandzi airport beach, Petite Terre, Mayotte). c) Syn-deposition normal faults in Strombolian volcanics of Anjouan (< 800 ka), seen from a road cut under construction (site AJ9). Stereo diagrams are equal area projections, lower hemisphere.

N135 ± 13.4° (Fig. 2a). Given their limited number, the five focal mechanisms from 1976 to 2017 yield only a low-quality reduced stress tensor (QR_{fm}: C), nevertheless also in strike-slip regime and with S_{Hmax} at N139 ± 7° (Fig. 2b), thus being compatible with the stress regime of the 2018- crisis.

4.2. Deformation and intrusion data

Examples of deformation structures observed in the field are given in Fig. 3. Paleostress inversions of these data are summarized in Table 2 and represented in Fig. 4. The full set of structural data is also provided as a Mendeley database [Famin and Michon, 2020], as stereo nets in Fig. S1, and as a site-by-site description of the observed structures in Table S2. A striking feature of our investigation of Mayotte is the abundance of deformation structures observed in the field (e.g. Fig. 3a). Over 730+ outcrop-scale faults and extensions fractures have been measured at 30 sites (Table S2), of which 20 sites yield acceptable paleostress tensors (Table 2). Most of the deformation structures consist in thrust or strike-slip faults (Fig. 3a), yet other structures such as folding or fracture schistosity also occur. Field-observed relationships and statistical analysis show that two populations of mechanically incompatible deformation structures coexist. The dominant population in terms of abundance, comprising > 450 structures found at 19 sites all-over Mayotte, yields reduced paleostress tensors indicative of thrust or strike-slip regimes with S_{Hmax} oriented NW-SE to N-S (Table 2, Fig. 4). The minor population, made of < 150 structures only found at 7 sites on the central part of the island, is mostly made of thrust faults compatible with WSW-ENE to *E*-W shortening. No clear chronological relationship between the two populations is observed, except at one site (MA19) where the dominant population postdates and reactivates the minor one (Table 2). Importantly, the dominant population can be found as capped by volcanic deposits of the Strombolian phase V aged of 800–200 ka (site MA16, Fig. 3a), or as cutting the latest phonolitic tephras of Petite Terre (site MA50, Fig. 3b), aged of less than 200 ka and possibly as young as 4 ka (Zinke et al., 2003; Pelleter et al., 2014). These chronological criteria indicate that deformation occurred from at least 800 ka to very recent times. A total of 167 intrusions (mostly subvertical dykes) has been measured at 6 sites in Mayotte, the majority being found in the less altered northern side of the island (Table 2). The main orientation of dykes is N150–160°, but a secondary N100–120° dyke trend is found on the northern shore of Mayotte (Fig. 4). These two dyke trends are mechanically compatible with paleostress tensors of the dominant population of deformation data. The final inversion of both the dominant population of deformation data and intrusions yields a strike-slip paleostress tensor of high quality (QR_{fm}: A) with S_{Hmax} at N160 ± 7° (Table 1, Fig. 2c). The final inversion of the minor population of deformation data yields a strike-slip paleostress tensor of lower quality (QR_{fm}: C) with S_{Hmax} at N074 ± 10° (Table 1, Fig. 2d).

In comparison with Mayotte, few deformation structures have been measured in Anjouan (130 faults at 5 sites) and Mohéli (89 faults at 3 sites), but this partly reflects the smaller amount of fieldwork allotted to these islands and also partly their high vegetation cover. Paleostress tensors obtained for Anjouan are in strike-slip and extensional regimes whereas those of Mohéli are dominantly in thrust regime, with S_{Hmax} oriented NNW-SSE or N-S on both islands (Table 2, Fig. 4). As for Mayotte, deformation is found even in the most recent (< 800 ka) Strombolian volcanic deposits of Anjouan and is even synchronous with those deposits (Fig. 3c). 77 and 31 dykes and sills were measured in Anjouan and Mohéli, respectively, with two preferential directions, N140–160° to N-S and N050–060° (Fig. 4). For Anjouan, the final inversion of deformation and intrusion data yields a paleostress tensor in extension regime with S_{Hmax} oriented N166 ± 9° (QR_{fm}: C, Table 1, Fig. 2e), whereas for Mohéli, the limited number of data only provides a poorly constrained tensor in between normal and strike-slip regimes, with an S_{Hmax} at N178 ± 5° (QR_{fm}: C; Table 1, Fig. 2f).

4.3. Spatial repartition of volcanic cones

Onshore and offshore mapping of volcanic cones in the GCVA area are illustrated in Figs. 5 and 6. The raw topographic and bathymetric grid without mapping is provided in Fig. S2. The volcanic alignments determined from the elongation and repartition of eruptive vents, and their reliability criteria, are given in Table 3. Onshore mapping reveals two different repartitions of eruptive vents (Fig. 5). The islands of Grande Comore and Anjouan, and to a lesser extent Mohéli, display a vent repartition following the topographic ridges of the islands, N005°, N142° and N153° for Grande Comore, N105° and N152° for Anjouan, and N115° for Mohéli. The island of Mayotte does not present any marked rift zone, and yet displays a general NNW-SSE repartition of its most recent volcanic activity (< 200 ka) from the north shore of the main island to the islet of Petite Terre (Fig. 4). The bathymetric data, only available for an area covering the east of Anjouan to the Geyser and Zélée banks, reveal the following additional features in the repartition of submarine eruptive vents (Figs. 5, 6): (1) The N105° and N152° rift zones of Anjouan have an offshore extent of at least ~10 km toward the east and the south, respectively. (2) The recent onshore volcanism on Mayotte is in fact the westward extremity of a N109° cone alignment extending at least 50 km offshore toward the new volcano and beyond. (3) Offshore volcanism north of Mayotte is delimited by a N135° axis (Fig. 6). (4) The four volcanic alignments of the Anjouan-to-Mayotte area delimit a sigmoidal pattern of preferential volcanic cone repartition (Fig. 6). (5) Two subparallel N135° and N136° lineaments of volcanic cones are observed along the Jumelles ridges, which confirms that these structures have focused Neogene-to-present volcanism. (6) A N101°-elongated swarm of volcanic cones is found south of the Geyser and Zélée banks and parallel to their N095° alignment, also confirming a Neogene-to-present volcanism along these structures.

5. Discussion

5.1. Stress and paleostress states in the Comoros archipelago

While earthquakes provide a snapshot of the present-day stress state of the Comorian lithosphere, deformation structures and intrusions give an integrated view of superficial, past stress fields over several million years. The question then arises as whether the two kinds of information can be compared in space at the scale of the entire GCVA, and in time at such different timescales. The spatial homogeneity of our dataset may first be tested among earthquake focal mechanisms only, which has the advantage of reducing the time interval considered. The average stress tensor from focal mechanisms of the 1976–2017 period all-over the GCVA (strike-slip faulting, S_{Hmax}: N139 ± 7°, subset 1 in Table 1) is consistent within uncertainty with the stress regime of the 2018- crisis (strike-slip faulting, S_{Hmax}: N135 ± 13.4°, subset 2 in Table 1). This consistency suggests that the stress field inferred from earthquakes is very homogeneous in the GCVA over the 1976–2018 period, before and during the volcanic and seismic crisis. Spatial comparisons may also be tested among average paleostress tensors on the three investigated islands. The remarkable homogeneity of the dominant S_{Hmax} in Mayotte (Fig. 4), and the absence of a radial or concentric pattern, clearly indicates that the paleostress state of this island is primarily of tectonic origin, and that volcanic activity or spreading play only a minor role in the deformation of the edifice. Extending the comparison to a wider spatial scale, the dominant average tensor of Mayotte and that of Mohéli are both in strike-slip regime whereas the average tensor of Anjouan is extensional. Despite this difference, the maximum horizontal stresses of these three average tensors are consistently oriented NNW-SSE (S_{Hmax}: N160 ± 7°, N166 ± 10°, and N178 ± 5°, subsets 3, 5, and 6 in Table 1, respectively), suggesting that paleostresses, as recorded in subaerial volcanism, are also relatively homogenous in space over the GCVA, further substantiating a regional tectonic origin. As the mean virtual geomagnetic pole for volcanic rocks from Mayotte,

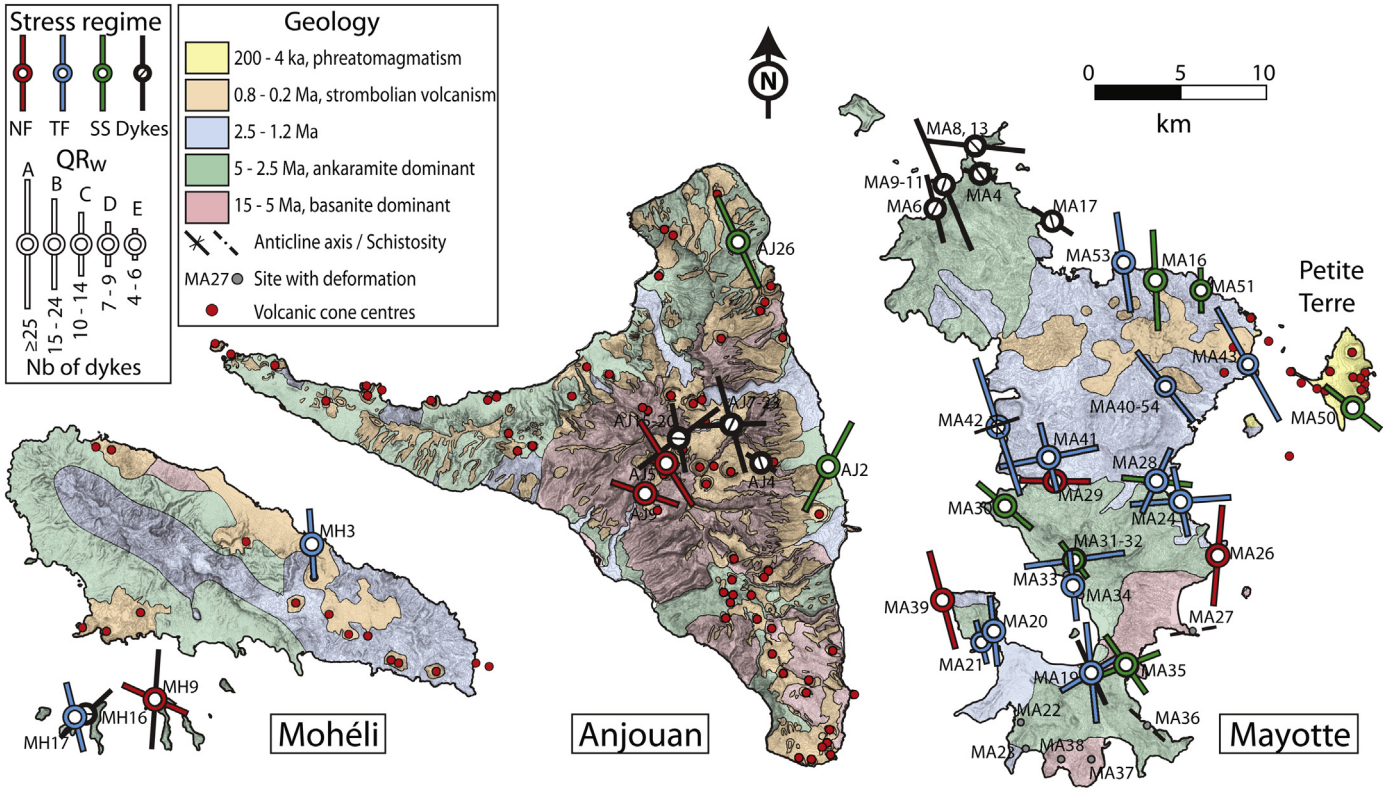

Fig. 4. Onshore spatial repartition of paleostress tensors and volcanic cones on the islands of Mayotte, Anjouan, and Mohéli. Paleostress data are represented as S_{Hmax} axes, the length of which is proportional to the quality of the inversion (QR_w) for faults or to the number of data measured in the field for dykes. Outcrops with observed deformation structures that could not yield acceptable paleostress tensors are also represented (see Table S2 for site descriptions). The geologic map of Mayotte is drawn according to the paleomagnetic map and phase subdivision of Nehlig et al. (2013). The geologic maps of Anjouan and Mohéli and their chronostratigraphies are from *Robineau* [pers. com.] and Nougier et al. (1986), respectively.

Anjouan, Mohéli and Grande Comore coincides with the present spin axis of the Earth (Hajash and Armstrong, 1972), it can be assumed that this regional paleostress field has not been disturbed by rotation of these islands.

The temporal homogeneity of our composite stress estimates may be tested by comparing closely-spaced paleostress and stress tensors. For instance, the closest deformation site from the 2018- seismic crisis is the one obtained at Petite Terre in tephras younger than 200 ka (site MA50, Fig. 3b). Deformation at this site yields a paleostress tensor (strike-slip, S_{Hmax}: N128 ± 5°, Table 2) consistent in both stress regime and orientation with the tensor obtained for the 2018- crisis, which suggests that focal mechanisms and deformation data in young (< 200 ka) volcanic rocks 50 km apart record a similar stress field.

Temporal comparisons may then be extended to longer timescales by considering jointly averaged paleostress tensors and earthquakes. In this respect, the dominant average paleostress tensor of Mayotte (subset 3 in Table 1, Fig. 2c) is relatively consistent with that of the 2018- crisis (subset 1, Table 1, Fig. 2a), although with a slightly higher S_{Hmax} strike. The average paleostress tensor of Anjouan (subset 5, Table 1, Fig. 2e) is very similar in stress regime and orientation to the focal mechanism of the 2011 Anjouan earthquake (Fig. 5). Likewise, the average paleostress tensor of Mohéli (subset 6, Table 1, Fig. 2f) is also mechanically compatible with the two focal mechanisms of the 2000 and 2016 earthquakes (Fig. 5).

These multiple cross-comparisons confirm an overall spatial and temporal agreement between earthquake, deformation, and intrusion data as markers of stress and paleostress estimates, which in turn suggests that the stress field of the GCVA has been relatively homogeneous over the studied area and since at least the period of Strombolian volcanism (≤ 0.8 Ma). This stress field is dominantly in strike-slip regime with a NW-SE maximum horizontal stress axis. Our results corroborate, with a considerably higher resolution, global plate stress models that predict a strike-slip or extension with a NW-SE S_{Hmax} in the Mozambique channel (Bird et al., 2008; Ghosh and Holt, 2012), and more recent geodetic strain rate models that consider the Comoros as a transitional zone between the EARS undergoing extension and Madagascar under transpression (Stamps et al., 2018). Our inversion results are also consistent with and earthquake focal mechanism inversions that yield a consistent NNW-SSE S_{Hmax} across East Africa (Delvaux and Barth, 2010).

Another element of our deformation data that remains to be discussed is the secondary paleostress tensor obtained in Mayotte (subset 4 in Table 1, Fig. 2d). This paleostress tensor is in strike-slip regime as the main tensor, but its maximum horizontal stress is almost perpendicular to that of the main tensor (Fig. 5). We note that this minor deformation is only found in the central part of Mayotte (Fig. 4). The lack of any convincing chronological criteria and the mutual crosscutting between the dominant and the minor populations of deformation data suggests that both occurred during the same time interval (Table 2). Repeated magma injections in a volcanic edifice are known to modify significantly the internal stress field of the edifice, and may possibly lead to permutations of stress and/or strain axes (Chaput et al., 2014, 2017). We therefore interpret this secondary set of deformation data as due to stress or strain permutations in the internal part of Mayotte.

5.2. *Distribution of latest volcanism*

Because small volcanic cones are rapidly eroded, these edifices represent the latest and most easily identified manifestation of volcanism. The repartition of volcanic cones may therefore be used as a proxy to infer the zones of preferential magma pathways in the crust. Onshore, cones corresponding to the phreatomagmatism of Mayotte are younger

Table 2
Paleostress tensor parameters obtained by inversion of deformation and intrusion structures on Mayotte, Anjouan, and Mohéli.

Site	Location	X UTM 38 L (m)	Y UTM 38 L (m)	Rock type	Volcanic period [a]	Rock age [b] (Ma)	Paleostress regime [c]	σ_1 dip/dip direction	σ_2 dip/dip direction	σ_3 dip/dip direction	Shmax (°)	QR_w	R	QR_t	n/n_t	Chronological criteria
Mayotte																
MA4	M'Tsangamboua stadium	511,580	8,597,055	Altered basalt	I	5–3.6	Dykes			01/193	103 ± 10.7	E			5/5	
MA6	M'Tsamboro point and beach	507,508	8,596,501	Ankaramite lavas	I	5–3.6	Dykes			06/079	169 ± 14.7	C			13/13	
MA8–13	Prefet's beach	509,240	8,599,110	Altered basalt	I	5–3.6	Dykes			01/186	096 ± 24.3	C			21/21	
MA9–10-11	Mtsahara point	508,262	8,597,845	Basalt lavas	I	5–3.6	Dykes			00/067	157 ± 15.3	C			107/108	
MA16	Kangani new quarry	519,852	8,592,287	Altered breccia above phonolite dome	III or IV	2.6–1.4	SS	18/352	63/222	19/088	176 ± 13.6	B	0.73	C	20/22	Faults capped by phase V
MA17	Bandraboua point	514,085	8,595,995	Olivine basalt lavas	I	5–3.6	Dykes			03/034	124 ± 9.2	D			7/7	
MA19	Chiroungui kaolinite cave	516,301	8,569,593	Argilised phonolite dome	II or older	> 3.2	Dykes			06/067	157 ± 9.7	C			11/11	Altered
							TF	11/242	04/332	78/084	058 ± 21.8	C	0.73	C	16/52	Cut dykes and alteration
							TF	11/175	34/272	54/070	174 ± 6.9	B	0.09	C	27/52	Reactivate previous faults
MA20	Mzouazia	510,741	8,571,973	Argilised basalt	II to III	3.4–2.5	TF	13/173	23/077	63/289	174 ± 7.3	C	0.26	C	17/21	
MA21	Bambo West pass	510,253	8,571,232	Argilised tephra	II to III	3.4–2.5	TF	07/165	07/074	80/303	166 ± 19.9	D	0.5	E	9/9	
MA24	Iloni point	521,171	8,579,856	Argilised pyroxene basalt	I to IV	4.5–1.4	TF	01/265	10/355	80/168	085 ± 12.6	B	0.17	B	37/92	Mutual crosscutting
							TF	03/350	08/259	82/104	169 ± 6.8	C	0.29	C	28/92	Mutual crosscutting
MA26	Hamouro point	523,924	8,576,686	Ankaramite lavas	III	2.6–1.8	NF	47/359	39/206	14/105	005 + 7.3	B	0.26	B	16/31	
MA28	Road N2 south of Tsoundsou II	519,963	8,580,799	Argilised basalt	III	2.6–1.8	SS	05/097	84/313	04/187	096 ± 7.1	C	0.28	C	16/31	Mutual crosscutting
							TF	04/025	00/115	86/219	024 ± 17.8	C	0.4	C	11/31	Mutual crosscutting
MA29	Barakani Road N2	513,805	8,580,578	Argilised basalt	III	2.6–1.8	NF	78/254	10/100	05/009	091 ± 22.8	C	0.08	C	19/21	Faults cut alteration
MA30	Sada road CD5	511,422	8,579,135	Argilised basalt	II	3.5–3.2	SS	17/131	72/328	05/222	130 ± 13.8	C	0.1	C	10/11	Faults cut alteration
MA31–32	Trail north of Poroani	515,284	8,575,982	Argilised basalt	II	3.5–3.2	TF	02/083	14/174	76/346	083 ± 17.7	B	0.45	C	17/42	Faults cut alteration
							SS	05/324	77/209	11/055	143 ± 6.4	D	0.03	D	14/42	Reactivate previous faults
MA33–34	Poroani road CD5	514,635	8,575,199	Argilised basalt	II	3.5–3.2	TF	10/350	36/252	52/093	174 ± 12.6	C	0.64	C	13/26	
MA35	Bambo Est road N3	518,267	8,570,029	Argilised basalt	III or older	> 1.8	SS	02/069	80/326	10/160	069 ± 7.7	C			13/40	Mutual crosscutting
							SS	11/327	64/080	23/232	145 ± 7.4	C	0.26	C	13/40	Mutual crosscutting
MA39	Boueni point	507,860	8,573,697	Altered ankaramite	II or III	3.4–1.8	NF	77/077	01/344	13/254	161 ± 38.3	B	0.1	E	15/17	Faults cut alteration
MA40–54	Doujani quarry	521,261	8,585,588	Altered phonolite dome	III	2.6–1.8	TF	11/140	12/048	73/271	141 ± 14.5	B	0.31	B	16/37	Faults cut alteration
MA41	Chiconi village	513,181	8,581,261	Argilised pyroxene basalt	III	2.6–1.8	TF	05/079	12/348	77/192	079 ± 6.1	B	0.4	B	19/47	Mutual crosscutting
							TF	24/165	19/066	59/301	167 ± 8.7	C	0.2	C	15/47	Mutual crosscutting
MA42	Tsingoni bay	511,059	8,583,782	Phonolite dome	III or IV	2–1.4	TF	15/166	03/257	74/359	161 ± 36.3	A	0.75	B	25/30	Serpentine in faults
MA43	Mamoudzou port	525,273	8,587,179	Argilised pyroxene basalt	III	2.6–1.8	TF	09/153	02/243	80/346	151 ± 28	A	0.72	A	25/41	Faults cut alteration

(*continued on next page*)

Table 2 (*continued*)

Site	Location	X UTM 38 L (m)	Y UTM 38 L (m)	Rock type	Volcanic period [a]	Rock age [b] (Ma)	Paleostress regime [c]	σ_1 dip/dip direction	σ_2 dip/dip direction	σ_3 dip/dip direction	Shmax (°)	QR_w	R	QR_t	n/n_t	Chronological criteria
MA50	Airport beach	531,345	8,585,038	Phonolitic tephra	VI	< 0.2	SS	01/129	89/304	00/039	128 ± 4.4	C	0.08	C	34/46	
MA51	Koungou quarry	522,540	8,591,283	Phonolite dome	III	2.6–1.8	SS	30/179	59/004	02/270	179 ± 3.9	D	0.49	D	6/10	
MA53	Longoni port	518,248	8,593,196	Argilised pyroxene basalt	III	2.6–1.8	TF	12/180	29/277	58/070	172 ± 16.1	B	0.72	B	17/41	Faults cut alteration
Anjouan																
AJ2	Bambao road	448,171	8,648,094	Altered basalt	Middle or Younger Series	4–1.5	SS	15/030	62/150	23/294	028 ± 7.7	B	0.31	B	15/36	Faults cut alteration
AJ4	Koni Djodjo road	444,620	8,648,393	Altered cpx + ol basalt	Middle Series	4–2.5	Dykes			01/031	121 ± 7.1	D			6/6	Altered dykes
AJ5	Road from Dindri to Magnasini	439,325	8,647,915	Lateritized basalt	Middle or Younger Series	4–1.5	NF	84/336	06/148	01/238	148 ± 12.8	B	0.39	B	21/52	Faults cut alteration
AJ9	Road from Dindri to Magnasini	437,794	8,646,678	Basaltic tephras	Recent cones	< 0.5	NF	88/349	01/102	02/192	102 ± 48.4	C	0.91	C	13/13	Fault *syn*-deposition
AJ15–20	Main river in Dindri valley	439,620	8,649,724	Gabbro pluton	?	> 10?	Dykes			02/325	055 ± 9.9	C			21/36	Main population
							Dykes			19/260	169 ± 9.8	C			11/36	Secondary population
AJ7–23–24-25	Tsimbeo	442,683	8,650,415	Quartzite massif and gabbro pluton	?	> 10?	Dykes			32/249	144 ± 35	C			18/30	Main population
							Dykes			10/000	088 ± 18.6	C			11/30	Secondary population
AJ26	Road from Hajoho to Jamilimé	443,850	8,661,979	Lateritized basalt	Younger Series	2.5–1.5	SS	09/157	79/297	07/066	156 ± 7.8	B	0.64	B	15/21	Faults cut alteration
Mohéli																
MH3	Road south of Djoiézi	367,879	8,638,807	Lateritized basalt	Younger Series	2.5–1.5	TF	16/356	11/263	71/139	176 ± 8.1	C	0.13	C	16/33	Faults cut alteration
MH9	Ouenefou Ilet	358,698	8,629,536	Oceanite an ankaramite lavas	Middle Series	4–2.5	Dykes			33/285	003 ± 23.9	C			20/20	
							NF	51/286	37/125	10/028	114 ± 12.8	C	0.5	C	40/44	Faults cut dykes
MH16–17	West ilet	354,860	8,628,793	Oceanite an ankaramite lavas	Middle Series	4–2.5	Dykes			03/317	047 ± 11.1	C			11/11	
							TF	04/346	03/077	85/205	166 ± 9.4	C	0.05	C	10/16	

[a] The volcanic periods of Mayotte, Anjouan, and Mohéli refer to the chronostratigraphic subdivisions of Nehlig et al. (2013) and Nougier et al. (1986), respectively.
[b] Rock ages are inferred from the chronostratigraphic scale or from literature radiometric dating in the vicinity of observation sites.
[c] Abbreviations TF, SS, NF, and NS refer to thrust, strike-slip, normal, and hybrid faulting, respectively.

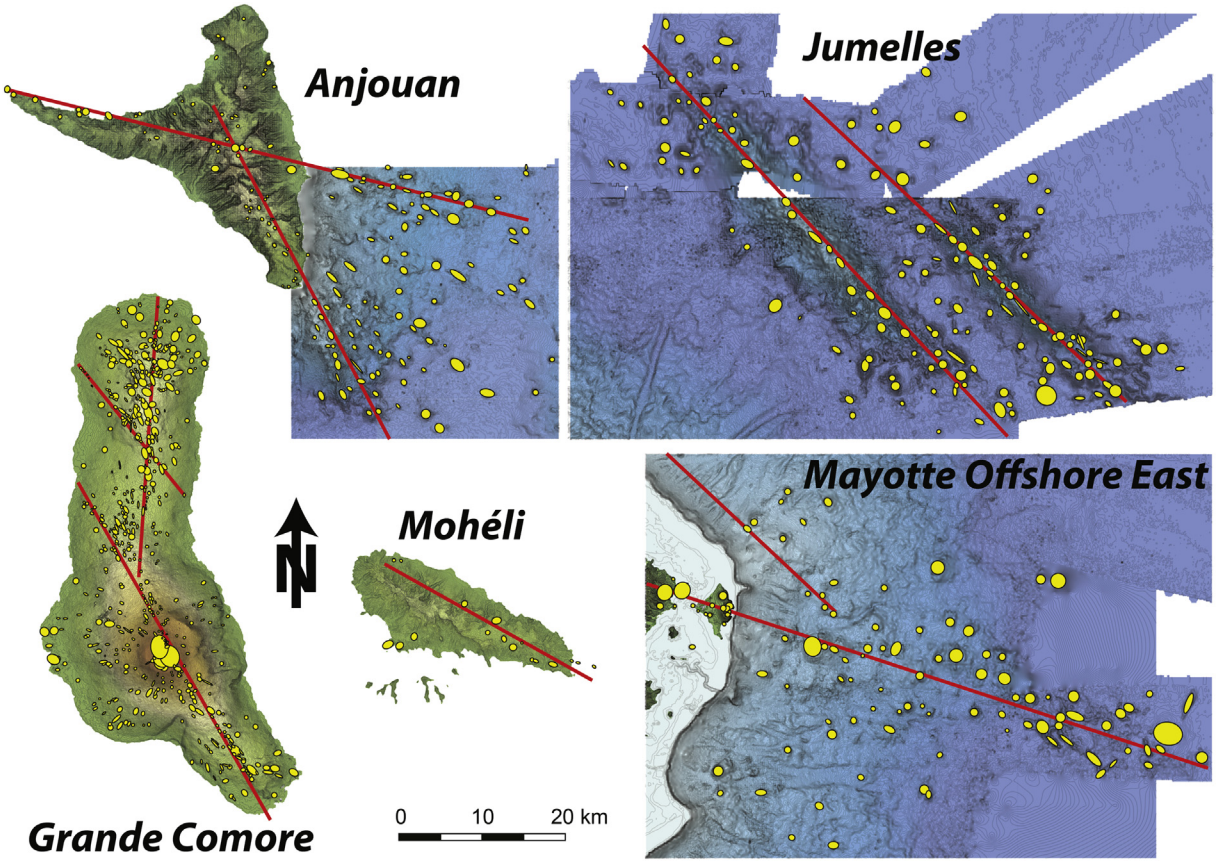

Fig. 5. Best-fit ellipses (in yellow) representing volcanic cone shapes onshore and offshore, and best-fit lines (in red) obtained by Deming regression analysis of cone centres, following the method of Paulsen and Wilson (2010). See Table 3 for cone alignment parameters. (For interpretation of the references to colour in this figure legend, the reader is referred to the web version of this article.)

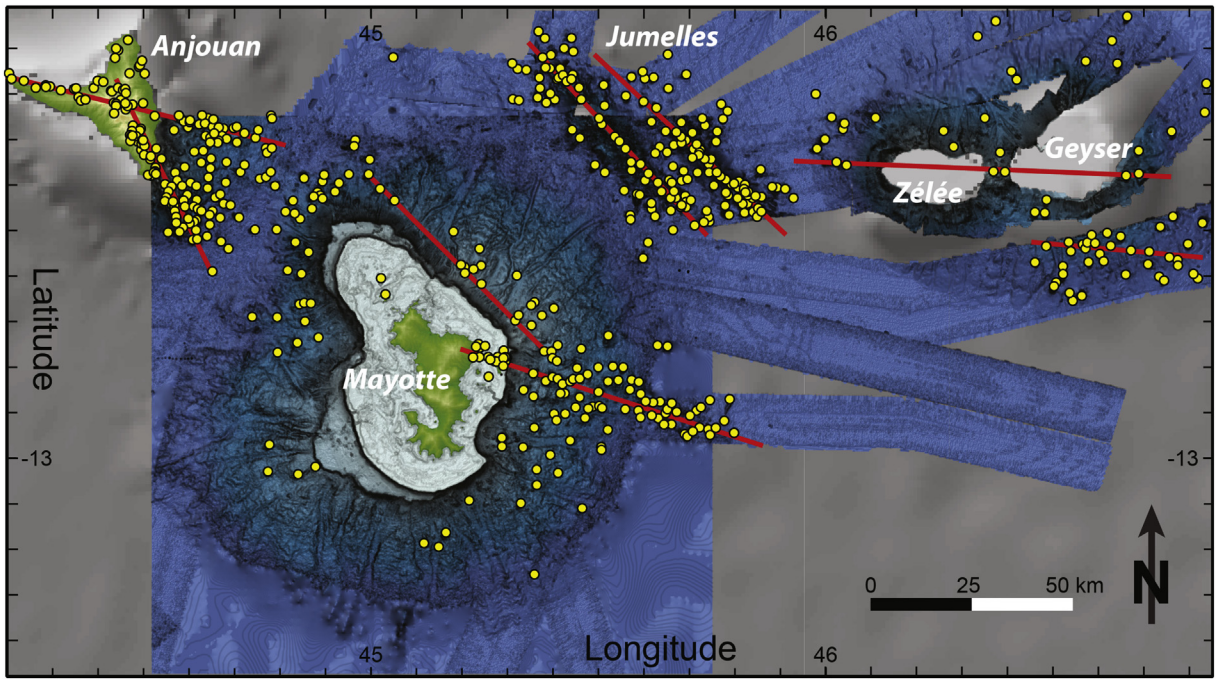

Fig. 6. Onshore and offshore repartition of volcanic cones in the Anjouan-to-Geyser area. For the sake of graphic representation, the yellow dots represent the centres of cones and are not fitted to cone sizes and shapes, as opposed to the ellipses of Fig. 5. The red lines represent the best-fit of cone alignments, as in Fig. 5. The topographic/bathymetric grid without cone mapping is provided in Fig. S2. (For interpretation of the references to colour in this figure legend, the reader is referred to the web version of this article.)

Table 3
Parameters of volcanic alignments.

Volcanic vent alignment	# vents included in regression	Average shape ratio of elongated vents	Standard deviation best-fit line distance (m)	Standard angular deviation vent long axes (°)	Alignment length (km)	Alignment azimuth (°N)	Alignment grade
Grande Comore north	61	1.7	483	23	22	142	A
Grande Comore N-S rift zone	177	1.6	709	23	36	5	A
Grande Comore south rift zone	194	1.6	739	19	48	153	A
Mohéli	12	1.4	1413	27	44	115	C
Anjouan N-S rift zone	63	1.5	733	18	52	152	A
Anjouan *E*-W rift zone	48	1.5	608	22	71	105	A
Mayotte offshore north	23	1.2	1034	19	60	135	C
Mayotte offshore east	39	1.4	615	16	78	109	A
Jumelles west	40	1.4	824	18	60	136	B
Jumelles east	43	2	1220	17	56	135	B
Geyser-Zélée banks	11	2.1	839	6	93	95	C
South of Geyser	26	1.2	1518	27	41	101	C

than 200 ka, while cones corresponding to the Strombolian volcanism of Mayotte and Anjouan are younger than 800 ka, and vents and fissures from Grande Comore are younger than 130 ka (see Pelleter et al., 2014 for a review of radiometric ages). On the offshore zones of the GCVA, the age of volcanic cones is unknown, yet submarine edifices of similar shapes have been dated at up to 8.5 Ma elsewhere (e.g. Janin et al., 2011). It must therefore be kept in mind that volcanic morphologies are much better preserved offshore than onshore. The field observation of dykes somewhat compensates this possible temporal bias, because it provides complementary information about onshore magma pathways and weakness zones over longer timescales than volcanic cones. On Mayotte for instance, the comparison of cone and dyke data suggests that the alignment of phreatomagmatic vents of Petite Terre may be prolonged westward along the northern shore of the island (Fig. 4).

Taken together, cones and dykes reveal that two directions of preferential volcanism – and hence of magma pathways – dominate the GCVA (Fig. 7). The first direction is made of N105 ± 10°, up to 100 km-long lineaments, represented by the Geyser – Zélée banks and by the volcanic alignment on their southern flanks, by the cone and dyke alignment running from the new submarine volcano to the northern shore of Mayotte, by the western rift zone of Anjouan prolonged offshore to the east, and by the elongated shape and volcanic alignment of Mohéli. The second direction is made of less than 60 km-long, N145 ± 10° lineaments such as the Jumelles seamounts, the main dyke orientation of Mayotte or the cone alignment on its northern submarine slope, the principal rift zone in Anjouan onshore and offshore, and also by two of the three Grande Comore lineaments. Importantly, these N145° segments are arranged in an *en échelon* fashion. Overall, volcanic alignments identified in the GCVA depict a roughly E-W zone of preferential volcanism and crustal weakness, in which the long N105° and shorter N145° segments form a rhombohedral geometry dipping east. The sigmoidal shaped repartition of preferential volcanism of Mayotte and Anjouan occupies a central position in this array of crustal weaknesses.

5.3. Comparison of stresses and volcanism

The superposition of stress and paleostress fields on the map of volcanic cone and dyke alignments reveals two important additional features (Fig. 7). First, the general orientation of past and present S_{Hmax} makes an acute angle with the longest, N105° volcanic lineaments, and is also parallel to the shorter *en échelon* N145° lineaments. Second, the rhombohedral geometry of these lineaments is mechanically consistent with the strike-slip stress or paleostress regimes. These two features lead us to interpret the GCVA as a broad (~150 km wide), E-W- to ESE-WNW-trending zone of distributed right-lateral wrenching. In this broad deforming domain, the major N105° volcanic structures are in the configuration of Riedel shear zones whereas the *en échelon* N145° segments occupy the position of extension fractures parallel to the average S_{Hmax} (Fig. 7). Given the width of the sheared domain and the absence of obvious mature faults throughout the studied area, we propose that right-lateral tear is still in an incipient state of strain localization. Deformation in the Mozambique channel is thus not as diffuse as proposed by Kusky et al. (2010). In this nascent deformation zone, the alignments of Mayotte and Anjouan represent perhaps the most evolved set of Riedel shears and extension fractures, between which the sigmoidal repartition of volcanic cones might be interpreted as a pull-apart or strike-slip duplex in the right-lateral shear zone. The new submarine volcano and the associated seismic crisis, located at the eastern tip of this sigmoidal pattern, suggest that deformation is still propagating SE, away from this growing structure. Following this interpretation, the lower (~N135°) azimuth of S_{Hmax} in the area of the 2018- seismic swarm than in Mayotte, Anjouan and Mohéli (~N160°) could result of stress concentration at the tip of the N105° segment propagating to the SE.

An important question that arises is whether these deformation structures are newly-formed or whether they reactivate the pre-existing fabric of the crust. Oceanic transform faults in the Somalia basin, north of the Comoros archipelago, provide N140–150° inherited structures (Phethean, 2016) candidate to reactivation as extension fractures. However, the N105° Riedel-like lineaments cannot come from an oceanic fabric, and require either neoformation, or a more complicated scenario like the reactivation of a E-W-trending passive margin. In this respect, the geodynamics of the Comoros area might be comparable to that of the Canary archipelago, also interpreted as a mantle anomaly interacting with the passive margin of western Africa under strike-slip tectonics (e.g. Anguita and Hernan, 2000).

Another open question is why deformation localizes in tandem with volcanism in the Comoros archipelago. Given the EM isotopic flavour of Grande Comore (Class et al., 2009), it is likely that a plume-related thermal anomaly weakens the lithosphere beneath this island. However, the other islands are more influenced by DMM and HIMU mixing, which implies more lithospheric melting sources. Deformation might play a feedback role in this dual signature, by weakening the lithosphere away from the mantle plume head, thus favouring the rise of melts related to the thermal anomaly but unconnected to the EM source. This scenario allows DMM-HIMU volcanism to occur simultaneously with EM volcanism along the zone of localized deformation, which better explains the present-day volcanic activity of the GCVA than the hotspot trail model.

The GCVA is a volcanic and seismic zone that connects the EARS to

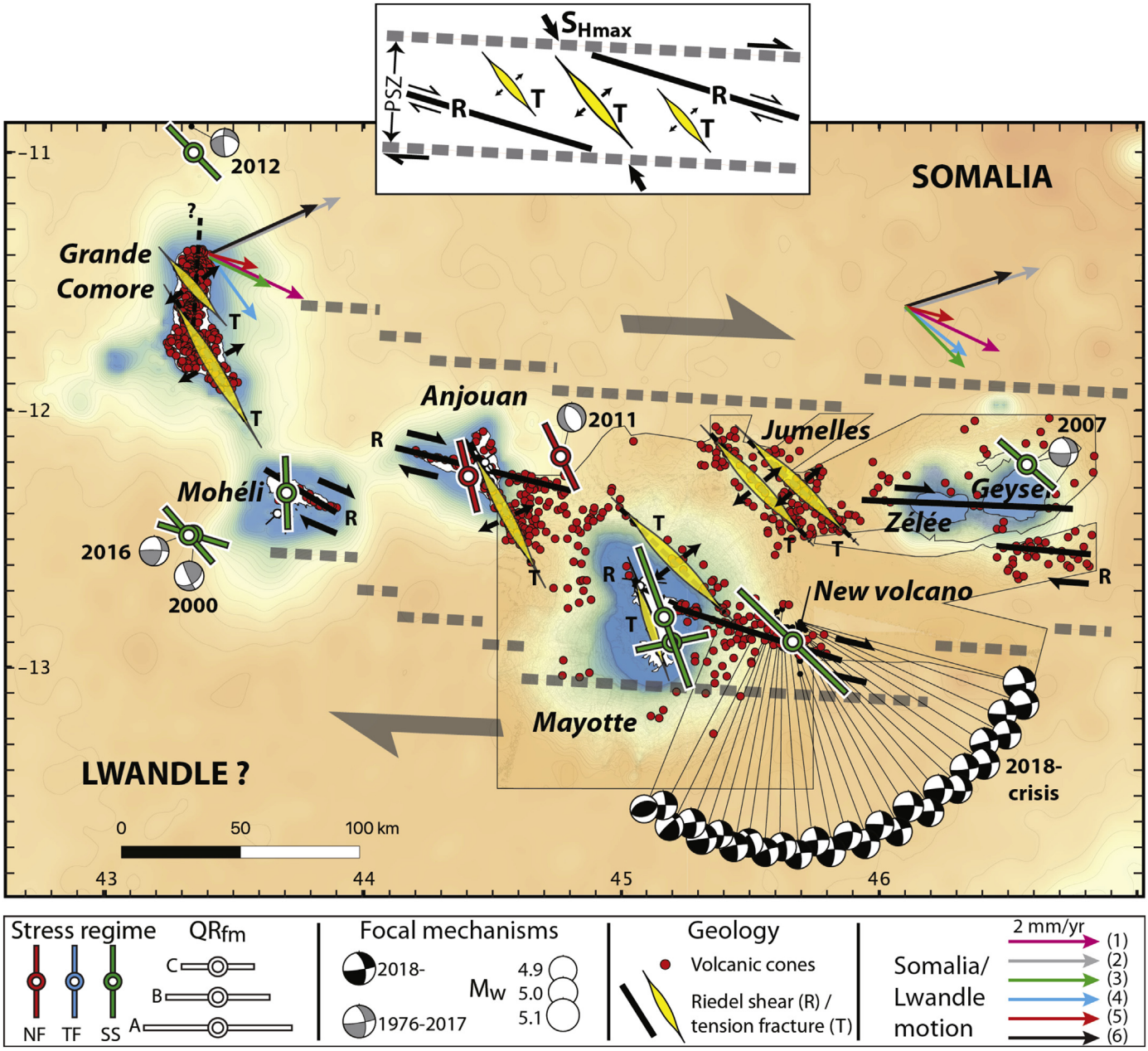

Fig. 7. Tectonic map of the Comoros archipelago, showing stress and paleostress regimes as S_{Hmax} axes proportional to the quality of their determination (QR_{fm}), focal mechanisms prior to and during the ongoing seismic and volcanic crisis, volcanic cones, and alignments of volcanic cones and dykes. Also represented are motion vectors of the Somalia plate relative to a fixed Lwandle block for different plate motion models, assuming the Comoros archipelago as built on a plate boundary (1- (Horner-Johnson et al., 2007); 2- GEODVEL, (Argus et al., 2010); 3- GRSM v2.1, (Kreemer et al., 2014); 4- (Saria et al., 2014); 5- (Graham et al., 2018); 6- T25M, Wang et al., (2018)). The inset represents our interpretation of the study area as a right-lateral principal shear zone (PSZ) with secondary Riedel shears (R) and extension fractures (T).

the Tertiary-to-Quaternary volcanism and rifting of northern and central Madagascar (Fig. 1b). This connection to known plate boundaries makes of the GCVA a candidate for the northern limit between the Lwandle and Somalia plates, a limit recently used by Stamps et al. (2018). Our study further substantiates this idea by identifying the GCVA as a zone of right-lateral tear in the lithosphere. Considering the GCVA as a plate boundary yields large (almost 90°) angular variations in the predicted velocity field of Somalia relative to Lwandle in the Comoros area depending on the chosen plate model (Fig. 7). This is quite unsurprising because the lack of geodetic data on the Lwandle plate – mostly covered by oceans, and the small relative motion of the two plates, hampers a precise determination of Euler vectors (Horner-Johnson et al., 2007; Morgan and Phipps Morgan, 2007; Saria et al., 2014; Graham et al., 2018; Wang et al., 2018). Despite these limitations, all the models yield a Somalia plate motion of 1.1–2.5 mm/yr toward the ENE to SE relative to Lwandle in the Comoros area, which implies a dextral transtension to transpression along the GCVA. Our findings are consistent with this predicted relative plate motion. We note that plate motion models based on interseismic geodetic data or spreading rates along the South West Indian Ridge (e.g. Horner-Johnson et al., 2007; Saria et al., 2014; Graham et al., 2018) predict pure strike-slip or transpression along the GCVA, in better match with our proposed kinematics than those based on hotspot tracks (e.g. Morgan and Phipps Morgan, 2007; Wang et al., 2018). In this respect, it is important to recall that the Comoros archipelago is always an outlier hotspot track in these later models.

Based on all these lines of evidence (localization of volcanism, seismicity, and deformation, stress and paleostress fields, and plate kinematics), we conclude that the GCVA is more consistent with being the northern Lwandle-Somalia plate boundary than being a hotspot track. This plate boundary, initiated by a mantle thermal anomaly, is probably still in an incipient state of strain localization, the reason why its interpretation remained so controversial. The connection of this dextral strike-slip fault zone to the Kerimba grabens toward the west, and to the volcanism and grabens of northern Madagascar toward the east, will require further investigations to improve the location and kinematics of the Lwandle-Somalia boundary. More work is also needed to determine whether this limit is in transtension, pure strike-slip or transpression. Nevertheless, the practical implication of our study is that the GCVA, and particularly the Mayotte-Anjouan area, is a tectonically active zone. The likeliness and consequences of a right-lateral reactivation of the ~N110° structure east of Mayotte should therefore be included in any hazard assessment plan of the region, as is its volcanic activity.

6. Conclusion

Our combined stress inversion of earthquake focal mechanisms, deformation structures, and intrusions, reveals that the Comoros archipelago undergoes a generalized dextral shear deformation with a NW-SE-directed maximum horizontal stress, active since at least the past million years. From the examination of digital surface models and intrusion data, we identified two trends of preferential volcanic vents repartition onshore and offshore in the Comoros area: a N105° trend of up to 100 km-long lineaments, and a N145° trend of ≤60 km-long, *en échelon* segments. Taken together, our results indicate that the Comoros archipelago is an approximately E-W zone of right-lateral wrenching of the lithosphere. Among the major implications of this finding, one is that the volcanic chain running from Northern Madagascar to the Comoros is not a classical hotspot track, which explains why it is always an outlier in absolute plate motion models based on hotspot trends. Rather, we propose that the Comoros archipelago represents the northern boundary between the Lwandle and Somalia plates. This E-W, right-lateral boundary, consistent with plate motions, is still in an immature state, the reason why it was interpreted as a hotspot trail.

Supplementary data to this article can be found online at https://doi.org/10.1016/j.tecto.2020.228539.

Funding

This research was partly funded by the CNRS/INSU TELLUS "MAYVOLTE" grant.

Acknowledgment

We wish to express our warm thanks to the Parc National Marin de Mohéli and its executive director Mr. Lailina Daniel, for the logistical help provided during the field work. We also thank Zakaria Gou for his guidance in the field of Anjouan. Structural data are available in a Mendeley database [Famin and Michon, 2020]. This IPGP contribution 4142.

References

Angelier, J., 1984. Tectonic analysis of fault slip data sets. J. Geophys. Res. 89, 5835. https://doi.org/10.1029/JB089iB07p05835.

Anguita, F., Hernan, F., 2000. The Canary Islands origin : a unifying model. J. Volcanol. Geotherm. Res. 103, 1–26.

Argus, D.F., Gordon, R.G., Heflin, M.B., Ma, C., Eanes, R.J., Willis, P., Peltier, W.R., Owen, S.E., 2010. The angular velocities of the plates and the velocity of Earth ' s Centre from space geodesy DATA AND ERROR BUDGET. Geophys. J. Int. 180, 913–960. https://doi.org/10.1111/j.1365-246X.2009.04463.x.

Barth, A., Wenzel, F., Giardini, D., 2007. Frequency sensitive moment tensor inversion for light to moderate magnitude earthquakes in eastern Africa. Geophys. Res. Lett. 34, 1–5. https://doi.org/10.1029/2007GL030359.

Bertil, D., Regnoult, J.-M., 1998. Seismotectonics of Madagascar. Tectonophysics 294, 57–74. https://doi.org/10.1016/S0040-1951(98)00088-2.

Bird, P., Liu, Z., Rucker, W.K., 2008. Stresses that drive the plates from below : definitions, computational path, model optimization, and error analysis. J. Geophys. Res. B Solid Earth 113, 1–32. https://doi.org/10.1029/2007JB005460.

Cesca, S., Letort, J., Razafindrakoto, H.N.T., Heimann, S., Rivalta, E., Isken, M.P., Nikkhoo, M., Passarelli, L., Petersen, G.M., Cotton, F., Dahm, T., 2020. Drainage of a deep magma reservoir near Mayotte inferred from seismicity and deformation. Nat. Geosci. 13, 87–93. https://doi.org/10.1038/s41561-019-0505-5.

Chaput, M., Famin, V., Michon, L., 2014. Deformation of basaltic shield volcanoes under cointrusive stress permutations. J. Geophys. Res. B Solid Earth 119, 274–301.

Chaput, M., Famin, V., Michon, L., 2017. Sheet intrusions and deformation of Piton des Neiges, and their implication for the volcano-tectonics of La Réunion. Tectonophysics 717, 531–546. https://doi.org/10.1016/j.tecto.2017.08.039.

Class, C., Goldstein, S.L., Shirey, S.B., 2009. Osmium isotopes in Grande Comore lavas: a new extreme among a spectrum of EM-type mantle endmembers. Earth Planet. Sci. Lett. 284, 219–227. https://doi.org/10.1016/j.epsl.2009.04.031.

Cucciniello, C., Tucker, R.D., Jourdan, F., Melluso, L., Morra, V., 2016. The age and petrogenesis of alkaline magmatism in the Ampasindava Peninsula and Nosy Be archipelago, northern Madagascar. Mineral. Petrol. 110, 309–331. https://doi.org/10.1007/s00710-015-0387-1.

Daniel, J., Dupont, J., Jouannic, C., 1972. Relations Madagascar-Archipel des Comores (Nord-Est du Canal du Mozambique). In: Sur la nature volcanique du banc de Leven. 274. Compte-Rendu l'Académie des Sci, Paris, pp. 1784–1787.

Davis, J.K., Lawver, L.A., Norton, I.O., Gahagan, L.M., 2016. New Somali Basin magnetic anomalies and a plate model for the early Indian Ocean. Gondwana Res. 34, 16–28. https://doi.org/10.1016/j.gr.2016.02.010.

Delvaux, D., Barth, A., 2010. African stress pattern from formal inversion of focal mechanism data. Tectonophysics 482, 105–128. https://doi.org/10.1016/j.tecto.2009.05.009.

Delvaux, D., Sperner, B., 2003. New aspects of tectonic stress inversion with reference to the TENSOR program. Geol. Soc. Lond., Spec. Publ. 212, 75–100. https://doi.org/10.1144/GSL.SP.2003.212.01.06.

Deville, E., Marsset, T., Courgeon, S., Jatiault, R., Ponte, J., Thereau, E., Jouet, G., Jorry, S.J., Droz, L., 2018. Active fault system across the oceanic lithosphere of the Mozambique Channel : Implications for the Nubia – Somalia southern plate boundary. Earth Planet. Sci. Lett. 502, 210–220. https://doi.org/10.1016/j.epsl.2018.08.052.

Dziewonski, A.M., Chou, T.-A., Woodhouse, J.H., 1981. Determination of earthquake source parameters from waveform data for studies of global and regional seismicity. J. Geophys. Res. 86, 2825–2852. https://doi.org/10.1029/JB086iB04p02825.

Ekström, G., Nettles, M., Dziewonski, A.M., 2012. The global CMT project 2004-2010: Centroid-moment tensors for 13,017 earthquakes. Phys. Earth Planet. Inter. 200–201, 1–9. https://doi.org/10.1016/j.pepi.2012.04.002.

Emerick, C.M., Duncan, R.A., 1982. Age progressive volcanism in the Comores Archipelago, western Indian Ocean and implications for Somali plate tectonics. Earth Planet. Sci. Lett. 60, 415–428.

Esson, J., Flower, M.F.J., Strong, D.F., Upton, B.G.J., Wadsworth, W.J., 1970. Geology of the Comores Archipelago, Western Indian Ocean. Geol. Mag. 107, 549–557. https://doi.org/10.1017/S0016756800058647.

Feuillet, N., Jorry, S., Crawford, W.C., Deplus, C., Thinon, I., Jacques, E., Saurel, J.-M., Lemoine, A., Paquet, F., Daniel, R., Gaillot, A., Satriano, C., Peltier, A., Aiken, C., Foix, O., Kowalski, P., Laurent, A., Beauducel, F., Grandin, R., Ballu, V., Bernard, P., Donval, J.-P., Géli, L., Gomez, J., Pelleau, P., Guyader, V., Rinnert, E., Besançon, S., Bertil, D., Lemarchand, A., Vanderwoerd, J., 2019. Birth of a large volcano offshore Mayotte through lithosphere-scale rifting. AGU fall Meet. V52D-01.

Famin, V., Michon, L., 2020. Data for: The Comoros archipelago: a right-lateral transform boundary between the Somalia and Lwandle plates. Mendeley Data V2. https://doi.org/10.17632/v2np7vm9pw.2.

Flower, M.F.J., 1972. Petrology of Volcanic Rocks from Anjouan, Comores Archipelago. Bull. Volcanol. 36, 238–250.

Franke, D., Jokat, W., Ladage, S., Stollhofen, H., Klimke, J., Lutz, R., Mahanjane, E.S., Ehrhardt, A., Schreckenberger, B., 2015. The offshore East African Rift System: Structural framework at the toe of a juvenile rift. Tectonics 34, 2086–2104. https://doi.org/10.1002/2015TC003922. Received.

Ghosh, A., Holt, W.E., 2012. Plate motions and stresses from global dynamic models. Science 335, 838–843.

Graham, S.E., Loveless, J.P., Meade, B.J., 2018. Global plate motions and earthquake cycle effects. G-Cubed 19, 2032–2048. https://doi.org/10.1029/2017GC007391.

Hajash, A., Armstrong, R.L., 1972. Paleomagnetic and radiometric evidence for the age of the Comores islands, west central Indian ocean. Earth Planet. Sci. Lett. 16, 231–236.

Hartnady, C.J.H., 2002. Earthquake hazard in Africa: perspectives on the Nubia-Somalia boundary. S. Afr. J. Sci. 98, 425–428.

Heidbach, O., Tingay, M., Barth, A., Reinecker, J., Kurfeß, D., Müller, B., 2010. Global crustal stress pattern based on the World stress Map database release 2008. Tectonophysics 482, 3–15. https://doi.org/10.1016/j.tecto.2009.07.023.

Heidbach, O., Rajabi, M., Cui, X., Fuchs, K., Müller, B., Reinecker, J., Reiter, K., Tingay, M., Wenzel, F., Xie, F., Ziegler, M.O., Zoback, Mary-lou, Zoback, Mark, 2018. The World Stress Map database release 2016 : crustal stress pattern across scales. Tectonophysics 744, 484–498. https://doi.org/10.1016/j.tecto.2018.07.007.

Horner-Johnson, B.C., Gordon, R.G., Argus, D.F., 2007. Plate kinematic evidence for the existence of a distinct plate between the Nubian and Somalian plates along the Southwest Indian Ridge. J. Geophys. Res. B Solid Earth 112, 1–12. https://doi.org/10.1029/2006JB004519.

Janin, M., Hémond, C., Guillou, H., Maia, M., Johnson, K.T.M., Bollinger, C., Liorzou, C.,

Mudholkar, A., 2011. Hot spot activity and tectonic settings near Amsterdam – St. Paul plateau (Indian Ocean). J. Geophys. Res. B Solid Earth 116, 1–17. https://doi.org/10.1029/2010JB007800.

King, R., Floyd, M., Reilinger, R., Bendick, R., 2015. GPS velocity field (MIT 2016.0a) for the East African Rift System [WWW Document]. Gener. By King al. Interdiscip. Earth Data Alliance (IEDA). https://doi.org/10.1594/IEDA/321764.

Kreemer, C., Blewitt, G., Klein, E.C., 2014. A geodetic plate motion and global strain rate model. G-Cubed 15, 3849–3889. https://doi.org/10.1002/2014GC005407.Received.

Kusky, T.M., Toraman, E., Raharimahefa, T., Rasoazanamparany, C., 2010. Active tectonics of the Alaotra–Ankay Graben System, Madagascar: possible extension of Somalian–African diffusive plate boundary? Gondwana Res. 18, 274–294. https://doi.org/10.1016/j.gr.2010.02.003.

Lacombe, O., 2012. Do fault slip data inversions actually yield "paleostresses" that can be compared with contemporary stresses? A critical discussion. Compt. Rendus Geosci. 344, 159–173. https://doi.org/10.1016/j.crte.2012.01.006.

Lemoine, A., Briole, P., Bertil, D., Roullé, A., Foumelis, M., Thinon, I., Raucoules, D., de Michele, M., Valty, P., 2020. The 2018-2019 seismo-volcanic crisis east of Mayotte, Comoros islands: seismicity and ground deformation markers of an exceptional submarine eruption. Geophysical Journal International, ggaa273. https://doi.org/10.1093/gji/ggaa273. In press.

Lund, B., Townend, J., 2007. Calculating horizontal stress orientations with full or partial knowledge of the tectonic stress tensor. Geophys. J. Int. 170, 1328–1335. https://doi.org/10.1111/j.1365-246X.2007.03468.x.

Maugé, L., Ségoufin, J., Vernier, E., Froget, C., 1982. Geomorphologie et origine des bancs du nord-est du canal du Mozambique - Ocean Indien occidental. Mar. Geol. 47, 37–55.

Michon, L., 2016. The volcanism of the Comores archipelago integrated at a regional scale. In: Bachèlery, P., Lénat, J.-F., Di Muro, A., Michon, L. (Eds.), Active Volcanoes of the Southwest Indian Ocean:Piton de La Fournaise and Karthala. Springer-Verlag, Berlin and Heidelberg, pp. 333–344.

Montaggioni, L.F., Nougier, J., 1981. Les enclaves de roches détritiques dans les volcans d'Anjouan (Archipel des Comores). Origine et interprétation dans le cadre de l'évolution du canal de Mozambique. Bull. Soc. Geol. Fr. 23, 595–601.

Morgan, W.J., Phipps Morgan, J., 2007. Plate velocities in the hotspot reference frame. In: Foulger, G.R., Jurdy, D.M. (Eds.), Plates, Plumes, and Planetary Processes. 430. Geol. Soc. of Am, Boulder, CO, pp. 65–78.

Nehlig, P., Lacquement, F., Bernard, J., Caroff, M., Deparis, J., Jaouen, T., Pelleter, A., Perrin, J., Prognon, C., Vittecoq, B., 2013. Notice de la carte géologique de Mayotte. BRGM/RP-61803-FR. pp. 135.

Nougier, J., Cantagrel, J.M., Karche, J.P., 1986. The Comores archipelago in the western Indian Ocean : volcanology, geochronology and geodynamic setting. J. Afr. Earth Sci. 5, 135–145.

Paulsen, T.S., Wilson, T.J., 2010. Tectonophysics New criteria for systematic mapping and reliability assessment of monogenetic volcanic vent alignments and elongate volcanic vents for crustal stress analyses. Tectonophysics 482, 16–28. https://doi.org/10.1016/j.tecto.2009.08.025.

Pelleter, A., Caroff, M., Cordier, C., Bachèlery, P., Nehlig, P., Debeuf, D., Arnaud, N., 2014. Melilite-bearing lavas in Mayotte (France): an insight into the mantle source below the Comores. Lithos 208–209, 281–297. https://doi.org/10.1016/j.lithos.2014.09.012.

Phethean, J.J.J., 2016. Madagascar's escape from Africa: a high-resolution plate reconstruction for the Western Somali Basin and implications for supercontinent dispersal. G-Cubed 17, 5036–5055. https://doi.org/10.1002/2016GC006624.Received.

REVOSIMA, 2020. Bulletin de l'activité sismo-volcanique à Mayotte. Paris.

Rindraharisaona, E., Guidarelli, M., Aoudia, A., Rambolamanana, G., 2013. Tectonophysics Earth structure and instrumental seismicity of Madagascar : Implications on the seismotectonics. Tectonophysics 594, 165–181. https://doi.org/10.1016/j.tecto.2013.03.033.

Saria, E., Calais, E., Stamps, D.S., Delvaux, D., Hartnady, C.J.H., 2014. Present-day kinematics of the East African Rift. J. Geophys. Res. B Solid Earth 119, 3584–3600. https://doi.org/10.1002/2013JB010901.Abstract.

SHOM, 2016. MNT bathymetrique de la façade de Mayotte (Projet Homonim) [WWW Document].

Sperner, B., Zweigel, P., 2010. A plea for more caution in fault-slip analysis. Tectonophysics 482, 29–41. https://doi.org/10.1016/j.tecto.2009.07.019.

Sperner, B., Müller, B., Heidbach, O., Delvaux, D., Reinecker, J., Fuchs, K., 2003. Tectonic stress in the Earth's crust: advances in the World stress Map project. Geol. Soc. Lond., Spec. Publ. 212, 101–116.

Stamps, D.S., Calais, E., Saria, E., Hartnady, C., Nocquet, J.-M., Ebinger, C.J., Fernandes, R.M., 2008. A kinematic model for the East African Rift. Geophys. Res. Lett. 35, 1–6. https://doi.org/10.1029/2007GL032781.

Stamps, D.S., Saria, E., Kreemer, C., 2018. A Geodetic Strain Rate Model for the East African Rift System. Sci. Rep. 8, 1–8. https://doi.org/10.1038/s41598-017-19097-w.

Suter, M., Quintero, O., Johnson, C.A., 1992. Active faults and state of stress in the central part of the Trans-Mexican Volcanic Belt, Mexico. 1. The Venta de Bravo Fault. J. Geophys. Res. B Solid Earth 97, 11983–11993.

Tadono, T., Ishida, H., Oda, F., Naito, S., Minakawa, S., Iwamoto, H., 2014. Precise Global DEM Generation by ALOS PRISM. In: ISPRS Ann. Photogramm. Remote Sens. Spat. Inf. Sci. II, pp. 71–76.

Wang, S., Yu, H., Zhang, Q., Zhao, Y., 2018. Absolute plate motions relative to deep mantle plumes. Earth Planet. Sci. Lett. 490, 88–99. https://doi.org/10.1016/j.epsl.2018.03.021.

Zinke, J., Reijmer, J.J.G., Thomassin, B.A., 2003. Systems tracts sedimentology in the lagoon of Mayotte associated with the Holocene transgression. Sediment. Geol. 160, 57–79. https://doi.org/10.1016/S0037-0738(02)00336-6.